preprint of *Advanced Robotics 25 (2011) 537–562*

Effects of Impedance Reduction of a Robot for Wrist Rehabilitation on Human Motor Strategies in Healthy Subjects during Pointing Tasks

Nevio Luigi Tagliamonte* Maria Scorcia Domenico Formica
Domenico Campolo Eugenio Guglielmelli

N. L. Tagliamonte, D. Formica, M. Scorcia and E. Guglielmelli are with the Laboratory of Biomedical Robotics and Biomicrosystems, School of Biomedical Engineering, Università Campus Bio-Medico di Roma, Via Álvaro del Portillo, 21 - 00128 Roma, Italy.

D. Campolo is with the School of Mechanical & Aerospace Engineering, Nanyang Technological University, 50 Nanyang Avenue, Singapore.

**Corresponding author:* n.tagliamonte@unicampus.it

Abstract

Studies on human motor control demonstrated the existence of simplifying strategies (namely 'Donders' law') adopted to deal with kinematically redundant motor tasks. In recent research we showed that Donders' law also holds for human wrist during pointing tasks, and that it is heavily perturbed when interacting with a highly back-drivable state-of-the-art rehabilitation robot. We hypothesized that this depends on the excessive mechanical impedance of the Pronation/Supination (PS) joint of the robot and in this work we analyzed the effects of its reduction. To this end we deployed a basic force control scheme, which minimizes human-robot interaction force. This resulted in a 70% reduction of the inertia in PS joint and in decrease of 81% and 78% of the interaction torques during 1-DOF and 3-DOFs tasks. To assess the effects on human motor strategies, pointing tasks were performed by three subjects with a lightweight handheld device, interacting with the robot using its standard PD control (setting impedance to zero) and with the force-controlled robot. We quantified Donders' law as 2-dimensional surfaces in the 3-dimensional configuration space of rotations. Results revealed that the subject-specific features of Donders' surfaces reappeared after the reduction of robot impedance obtained via the force control.

keywords: Back-drivability, wrist robots, human motor control, neural kinematic constraints, force control.

1 INTRODUCTION

Rehabilitation robotics has become an emerging field in recent years and the potentialities of robot-mediated motor therapy is being widely investigated [1]–[7].

During traditional neurorehabilitation sessions the role of the patient is quite passive and the participation of the high-level structures of his nervous system are limited. On the other hand, robotic therapy allows subjects to perform active movements, thus promoting neurogenesis and neuroplasticity, and optimizing the functional recovery after neurological injuries [8, 9].

During therapy rehabilitation robots are meant to: *i)* provide assistance as needed, not to perturb voluntary movements, and to help completing tasks that patients are not able to perform autonomously; *ii)* apply, if required, resistive force fields to improve the efficacy of the treatment. During assessment robots have to be as transparent as possible in order to minimally interfere with human natural motor strategies. In this sense a high back-drivability, i.e. a low perceived mechanical impedance during user-driven motion, is of crucial importance. Therapy and assessment sessions can be interlaced, and assessment sessions may determine the amount of future therapy to be imparted; therefore, assessment may also have an indirect impact on therapy. The technological choices regarding the design of mechanical structure and control strategies for this kind of robots have to face several issues, such as safety, dynamical adaptability and biomechanical compatibility [10]. Nevertheless, besides biomechanical constraints, also the understanding of neural strategies behind human motor control (especially in presence of dynamic interactions) should be considered to define some indications for robots design.

In this regard, it has been shown that rehabilitation machines have to comply not only with 'hard' (*biomechanical*) constraints but also with 'soft' (*neural*) constraints [11], which are adopted by the brain to solve kinematic redundancy and to implement strategies for motor efficiency.

Studies on human motor control have demonstrated the existence of simplifying strategies adopted by the brain when dealing with kinematically redundant problems. Such strategies are often referred to as *Donders' law* or *Listing's law* for historical reasons, in relation to the early Donders' and Listing's studies on the eye movements. In a good approximation, the eye can be considered as a center-fixed sphere rotated by the action of 6 (i.e. 3 agonist-antagonist couples) Extra Ocular Muscles (EOMs). EOMs provide 3 DOFs kinematics allowing full mobility in the space of rigid body rotations with the only limitations given in terms of range of motion. When looking at some point in space, the gaze direction is fully determined but not the amount of ocular torsion about the line of sight. In other words, for a given line of sight, uncountably many eye configurations (torsions) exist which correspond to the same gaze direction.

In 1847, Donders experimentally found that for a given *steady* gaze direction there is only one eye configuration (*Donders' Law*) [12]. In other words, physiological eye configurations are described by a 2-dimensional surface embedded into the 3-dimensional space of eye configurations: a solution to redundancy. Two decades later, Listing and Helmholtz determinated that such a 2-dimensional surface is actually a plane: the eye assumes only those positions that can be reached from primary position

by a single rotation about an axis in the *Listing's plane*, which lies orthogonal to the gaze direction in primary position (*Listing's Law*) [12]. Listing's law is therefore a particular form of a more general Donders' law: the former prescribes a plane whereas the latter prescribes a generic surface. Hereafter we shall refer, in general, to Donders' law.

It had been debated for quite some time whether Donders' law was due to a biomechanical or a neural mechanism. It is now known that such a law holds during fixation, saccades, smooth pursuit, and vergence, but not during sleep and vestibulo-ocular reflex, suggesting that it is actively implemented by a neural mechanism [13]. Moreover, in the last two decades, Donders' law has been found to well apply to the head as well as to limb movements [14, 15].

Recent studies demonstrated that Donders' law applies also to wrist movements during pointing tasks (in which the three DOFs of the wrist are redundant) [16]. This study was conducted measuring wrist orientations during pointing movements using a lightweight *handheld* device, which introduces a negligible perturbation to the physiological movements. The three dimensional rotations vectors resulted well fitted by quadratic (Donders') surfaces, whose curvature expresses inter-subjects differences in motor strategies, thus denoting a personal 'style' in solving redundancy [16].

The same analysis was conducted in [11] with subjects performing similar pointing tasks while interacting with the InMotion^3 system (Interactive Motion Technologies, Inc.), a the state-of-the-art robot for wrist neurorehabilitation, specifically designed to comply with the biomechanical constraints, and providing a high level of back-drivability [17]. In this case no statistically significant difference was found between subjects, suggesting that the robot flattens out any personal motor strategy; in particular, it was hypothesized that the impedance of the most proximal joint of the robot, responsible for Pronation/Supination (PS) movements, was not low enough to comply with the neural constraints. In other terms the robot perturbs voluntary movements of the subjects, despite its high level of transparency.

The objective of this study is to analyze the effect of a reduced perceived impedance of the InMotion^3 system on human motor strategies during pointing tasks. Our work could allow to examine the effects of different levels of back-drivability on human natural movements and to point out which level can avoid the occurrence of constraining behaviors thus suggesting a new approach for the design of rehabilitation robots which, at the state of art, does not consider neural constraints but only biomechanical ones.

To this aim the handle of the robot was provided with a load cell and a basic force control scheme (with a null reference) was implemented to minimize the interaction force exerted by the user. This kind of approach has been already validated in [18] on a different platform, the MIT-MANUS system [1], in both simulation and experimental tests. In [18] a reduction of (mean and maximum) forces exerted by a subject during planar pointing tasks have been verified in different operative conditions, demonstrating the effectiveness of the chosen force control scheme in improving the system transparency.

In this work inertia, friction and gravity effects were estimated for the PS joint of the InMotion^3 system to be actively compensated for. The performance of the robot have been analyzed with and without the force control to verify the reduction of its mechanical impedance. Moreover, the reduction of forces/torques required to three healthy subjects to perform two different kinds of tasks (involving

respectively 1 or 3 DOFs movements) has also been measured.

The effect of the reduced impedance of the robot on human motor strategies during 3-DOFs pointing tasks has been analyzed, by assessing wrist rotations of three healthy subjects in three different testing conditions: movements with *i)* the handheld device, *ii)* the robot with its standard PD control with gains set to zero and *iii)* the force-controlled robot; for each experiment Donders' surfaces were calculated as performance index.

In section 2 a description of the InMotion^3 wrist robot is provided, while the force control scheme is described in section 3 together with the estimation of robot dynamic parameters and the calculation of kinematic operators used for its implementation. The effects of force control on robot transparency and on human wrist kinematics/neural motor strategies are presented in sections 4 and 5 respectively.

2 INMOTION^3 WRIST ROBOT

The InMotion^3 system [17] has three active DOFs: Pronation/Supination (PS), Abduction/Adduction (AA) and Flexion/Extension (FE). A differential mechanism is used to achieve AA and FE movements; PS rotations entail the sliding along a curve guide of the housing comprising the differential gearing and the AA and FE actuators (Fig. 1). In [17] a quantification of the three axis inertia, friction and gravity terms is provided showing that PS values are one order of magnitude higher with respect to the two other DOFs.

The robot is actuated by three DC motors which are equipped with rotary encoders; angle resolution measurement is 0.017 deg for the PS DOF and 0.026 deg for FE and AA DOFs.

At the basis of the handle two passive DOFs, a linear slider and a revolute joint, are used to comply with the anatomic characteristics of different subjects and also for a further adaptation of the robot to the axes of rotation of the human wrist (Fig. 1).

The robot is provided by the manufacturer with a PD + gravity compensation control scheme (which, for simplicity, will be referred as *PD control*) so to generate programmable viscoelastic torque fields to deliver forces or impart movements during therapy. In particular, it can be programmed to provide different levels of mechanical impedance by properly setting the control stiffness and damping parameters (see [17] for details on the standard control of the InMotion^3 system). The minimal impedance, with this control scheme, can be achieved when these parameters are both set to zero; in this case the only role of the motors is to compensate the gravity effect.

In this work we sensorized the robot handle, in order to implement a direct force control for a further reduction of the impedance of the robot PS joint. To this aim we decided to remove the linear slider and the passive revolute joint, whose movements could not be measured, and to collocate a load cell to the basis of the end effector (Fig. 2).

A 6 axes JR3 torque/force sensor (20E12A4-I25-EF 100N5, JR3 Inc. - force f.s.: 100 N; torque f.s.: 5 Nm) with external electronics was used. The six analog outputs of the sensor were directly connected to an acquisition board already present on the robot, which automatically synchronizes external signals

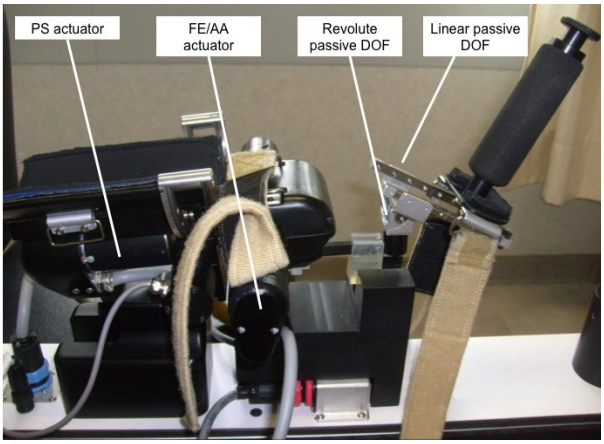

Figure 1: InMotion^3 wrist robot [17].

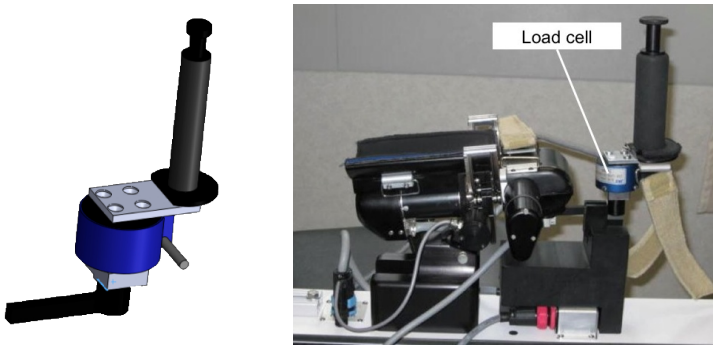

Figure 2: Integration of the force/torque sensor in the InMotion^3 system.

with the 200 Hz control software. The sampled signals have been multiplied by a calibration and decoupling matrix, provided by the manufacturer of the sensor.

3 FORCE CONTROL IMPLEMENTATION

The control algorithm used in this work is adapted from [19, 20]. It compensates robot dynamics (gravity, inertia and friction) and minimizes the end-point interaction force since a zero reference is imposed.

The equation of robot dynamics[1] can be expressed as:

$$\boldsymbol{B}(\boldsymbol{q})\ddot{\boldsymbol{q}} + \boldsymbol{b}\dot{\boldsymbol{q}} + \boldsymbol{g}(\boldsymbol{q}) = \boldsymbol{\tau} - \boldsymbol{J}^T(\boldsymbol{q})\boldsymbol{F}_{int} \tag{1}$$

where $\boldsymbol{F}_{int}$ represents the 6×1 vector of the generalized forces exerted by the user (with respect to the base frame), $\boldsymbol{b}$ is a 3×3 diagonal matrix of constant friction coefficients, $\boldsymbol{B}(\boldsymbol{q})$ is the 3×3 inertia matrix, $\boldsymbol{J}^T(\boldsymbol{q})$ is the 3×6 transpose Jacobian matrix, $\boldsymbol{g}(\boldsymbol{q})$ is the 3×1 gravity term and $\boldsymbol{\tau}$ is the 3×1 vector of control torques. Relation (1) is composed by three scalar equations, which refer to PS, AA and FE joints respectively; thus the vector of joint coordinates is $\boldsymbol{q} = [q_{PS}\ q_{AA}\ q_{FE}]^T$.

The implemented control law is:

$$\boldsymbol{\tau} = \hat{\boldsymbol{b}}\dot{\boldsymbol{q}} + \hat{\boldsymbol{g}}(\boldsymbol{q}) + \boldsymbol{J}^T(\boldsymbol{q})\boldsymbol{F}_{int} + \hat{\boldsymbol{B}}(\boldsymbol{q})\boldsymbol{K}_P\boldsymbol{J}^T(\boldsymbol{q})(\boldsymbol{F}_d - \boldsymbol{F}_{int}) \tag{2}$$

where the symbol ˆ indicates an estimation of the corresponding vector or matrix, $\boldsymbol{F}_{int}$ indicates the 6×1 vector of generalized forces measured by the load cell and $\boldsymbol{K_P}$ is a 3×3 positive-definite diagonal gain matrix.

Force error can be indicated as $\boldsymbol{e}_f = \boldsymbol{J}^T(\boldsymbol{q})(\boldsymbol{F}_d - \boldsymbol{F}_{int})$, where $\boldsymbol{F}_d$ is the desired interaction force. By substituting (2) in (1), and assuming that robot dynamics are perfectly estimated, the force error dynamics becomes:

$$\boldsymbol{e}_f = \boldsymbol{K}_P^{-1}\ddot{\boldsymbol{q}} \tag{3}$$

Considering $\boldsymbol{M} = \boldsymbol{K}_P^{-1}$, equation (13) can be expressed as:

$$\boldsymbol{e}_f = \boldsymbol{M}\ddot{\boldsymbol{q}} \tag{4}$$

If $\boldsymbol{F}_d$ is set to zero, equation (4) indicates that the system behaves like a free body with mass $\boldsymbol{M}$, so that increasing proportional gain (within stability margins) will reduce the perceived inertia.

[1] Coriolis and centrifugal effects have been neglected because of the low values of velocity involved in the wrist pointing tasks. Hereafter vectors and matrices will be reported in **bold** font.

Force control in (2) has been implemented only for the PS joint since the AA and FE joints are already highly back-drivable (their mechanical impedance is one order of magnitude smaller than the one of PS DOF, [17]); therefore, the control torques for the three DOFs can be written as follows:

$$\begin{cases} \tau_{PS} = \boldsymbol{\tau}[1\ 0\ 0]^T \\ \tau_{AA} = 0 \\ \tau_{FE} = 0 \end{cases} \tag{5}$$

with

$$\tau_{PS} = b_{PS}\dot{q}_{PS} + \tau_{PS}^g + [\boldsymbol{J}^T(\boldsymbol{q})\boldsymbol{F}_{int} + \hat{\boldsymbol{B}}(\boldsymbol{q})\boldsymbol{K}_P\boldsymbol{J}^T(\boldsymbol{q})(\boldsymbol{F}_d - \boldsymbol{F}_{int})][1\ 0\ 0]^T \tag{6}$$

where $\tau_{PS}^g = g_{PS}\sin(q_{PS})$ and b_{PS} are the gravity term and the friction coefficient of the PS DOF, respectively.

Indicating for simplicity $\tau_{PS}^{int} = [\boldsymbol{J}^T(\boldsymbol{q})\boldsymbol{F}_{int}][1\ 0\ 0]^T$ and $\tau_{PS}^{fb} = \hat{\boldsymbol{B}}(\boldsymbol{q})\boldsymbol{K}_P\boldsymbol{J}^T(\boldsymbol{q})(\boldsymbol{F}_d - \boldsymbol{F}_{int})][1\ 0\ 0]^T$ the final control torque for the PS DOF becomes:

$$\tau_{PS} = b_{PS}\dot{q}_{PS} + \tau_{PS}^g + \tau_{PS}^{int} + \tau_{PS}^{fb} \tag{7}$$

The implementation of the control scheme in (7) required the calculation of the robot kinematic operators and the estimation of its dynamical properties.

3.1 Robot kinematics

Since the robot native control is implemented only in the joint space, the calculation of the Jacobian matrix $\boldsymbol{J}(\boldsymbol{q})$, and of its transpose $\boldsymbol{J}^T(\boldsymbol{q})$, was necessary to map the torques/forces measured in the operative space in the corresponding actions on the joints. A schematic representation of the robot kinematics is provided in Fig. 3. Denavit-Hartenberg convention was used to select the frames of reference (the parameters are reported in Table 1) and to calculate the direct kinematics.

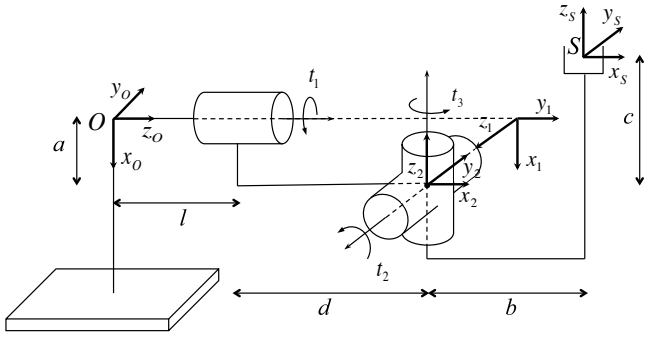

Figure 3: Schematic representation of the robot kinematics; frames of reference are selected using the Denavit-Hartenberg convention. We measured $a = 0.062$ m, $b = 0.158$ m, $c = 0.022$ m, $d = 0.120$ m, $l = 0.100$ m.

Table 1: Denavit-Hartenberg parameters for the kinematics of the InMotion^3 system.

Joint	a_i	d_i	α_i	θ_i
1	a	d	$-\pi/2$	t_1
2	0	0	$\pi/2$	t_2
3	b	c	0	t_3

The adjoint transformation [21] was used to map the vector of generalized forces from the the sensor coordinate frame (indicated with S in Fig. 3) to the global reference system (indicated with O in Fig. 3).

Let $\boldsymbol{p}_{os}$ be the 3×1 position vector of the origin of frame S from the origin of frame O and $\boldsymbol{R}_{os}$ the 3×3 rotation matrix describing the orientation of frame S with respect to frame O. This matrix is calculated as

$$\boldsymbol{R}_{os} = \boldsymbol{R}_{o1}(\mathrm{t}_1)\boldsymbol{R}_{12}(\mathrm{t}_2)\boldsymbol{R}_{2s}(\mathrm{t}_3) \tag{8}$$

being the $\boldsymbol{R_{i-1\ i}}(\mathrm{t}_i)$ matrix associated with the i-th rotation of the i-th frame with respect to the $(i-1)$-th one. Rotation matrices $\boldsymbol{R}_{o1}(\mathrm{t}_1)$ and $\boldsymbol{R}_{2s}(\mathrm{t}_3)$ indicate the orientation of frame 1 with respect to frame O and of frame S with respect to frame 2 respectively.

Indicating with g_{os} the pair $(\boldsymbol{p}_{os}, \boldsymbol{R}_{os})$ the matrix

$$\boldsymbol{Ad}_{g_{os}} = \begin{bmatrix} \boldsymbol{R}_{os} & \boldsymbol{p}_{os} \wedge \boldsymbol{R}_{os} \\ \boldsymbol{0} & \boldsymbol{R}_{os} \end{bmatrix} \tag{9}$$

associated with g_{os} is the adjoint matrix; its transpose transforms force vectors from the frame S the frame O as follows:

$$\boldsymbol{F}_{int} = \boldsymbol{Ad}^T_{g_{os}} \boldsymbol{F}^S_{int} \tag{10}$$

It has been assumed that the vector without superscripts is referred to the base frame.

3.2 Robot dynamics

3.2.1 Gravity term estimation

To estimate the gravity term for the PS joint, a correlation between different static configurations and the torques required to hold the robot in those positions was performed.

It is important to note that tests were carried out with AA and FE joints locked, being the actuators commanded to maintain their 0 reference position through high gains PD position control (in these conditions we verified a deviation from the rest position of FE and AA of less than of 3 deg which should not sensibly affect the estimation). The choice of neglecting the contribution of changes in AA

and FE configurations on the PS the gravity term is also adopted in [17] since the load produced by the handle on the PS joint is reasonably independent of the AA and FE orientations of the robot in the range of operation.

The robot was commanded to reach 10 positions (from -0.6 rad to $+0.6$ rad with respect to its rest position); PS actuator torques exerted to maintain these rotations in static conditions were evaluated. Fig. 4 shows an example of the PS torque and angle patterns during one estimation test of gravity term.

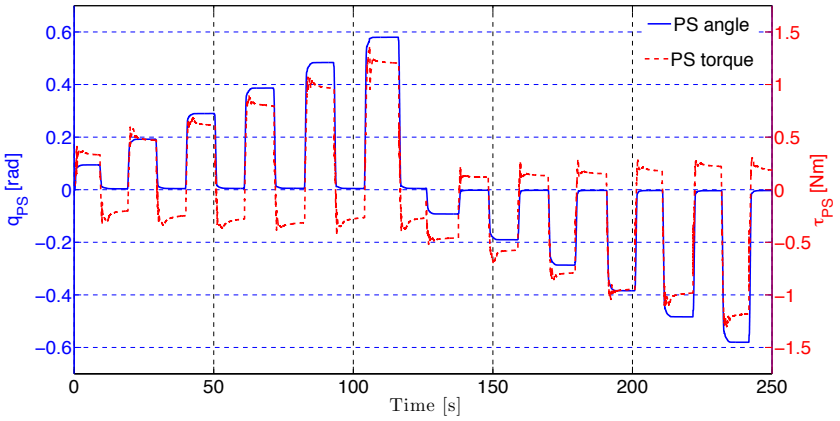

Figure 4: PS torque (dashed red) and angle (solid blue) patterns during one test for the gravity term estimation. Commanded angles varied from -0.6 rad to $+0.6$ rad with respect to the robot rest configuration.

As in [17] the gravity term has been assumed sinusoidally varying with PS angle so a linear regression between PS torque and the sin of the PS rotation was calculated for 5 trials. In Fig. 5 the collected data (static PS angles and torques for the 5 trials) are shown together with the best fitting curve.

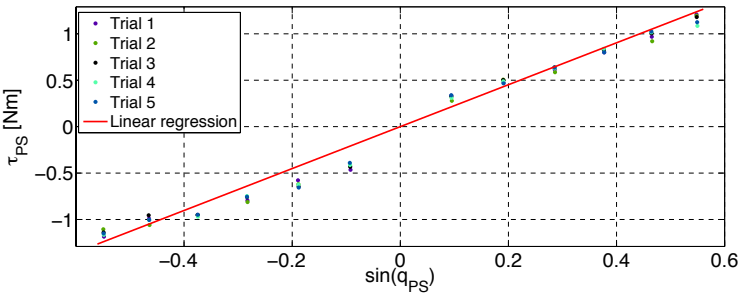

Figure 5: Linear regression between τ_{PS} and $\sin(q_{PS})$ static values for the estimation of the PS gravity term. The fitting curve slope is mediated on 5 trials. The resultant gravitational term is $\tau^g_{PS} = g_{PS}\sin(q_{PS}) = 2.254\sin(q_{PS})$.

The slope of the linear curve in Fig. 5, averaged on the 5 trials, was found to be $g_{PS} = 2.254 \pm 0.009$ Nm, with a mean R^2 of 0.980.

3.2.2 Inertia and friction estimation

To estimate inertia and friction terms the robot was back-driven to perform few rapid oscillating movements. The PS motor compensated the gravity effect (on the basis of the estimation reported in section 3.2.1) and the AA and FE actuators were commanded to maintain their rest positions through high gains PD position control; in these conditions a deviation of less than 3 deg for FE and AA was found. Force/torques exerted on the handle were recorded and their effect on the PS joint was calculated as follows:

$$\tau_{sens}^{PS} = [\boldsymbol{J}(\boldsymbol{q})^T \boldsymbol{Ad}_{g_{os}}^T \boldsymbol{F}_{int}^S][1\ 0\ 0]^T. \tag{11}$$

We estimated the inertia and friction terms for the PS joint by regressing the τ_{sens}^{PS} reported in (11) with angular velocities and accelerations of the PS DOF, as reported in the following equation:

$$\tau_{sens}^{PS} = \tau_0^{PS} + b_{PS}\dot{q}_{PS} + B_{PS}\ddot{q}_{PS} \tag{12}$$

The multivariable linear regression reported in (12) was calculated on 5 trials; the best fitting plane is shown in Fig. 6. We found $\tau_0^{PS} = 0.219 \pm 0.049$ Nm, $b_{PS} = 0.055 \pm 0.005$ Nm·s/rad and $B_{PS} = 0.012 \pm 0.001$ kg·m^2 with a mean R^2 of 0.942.

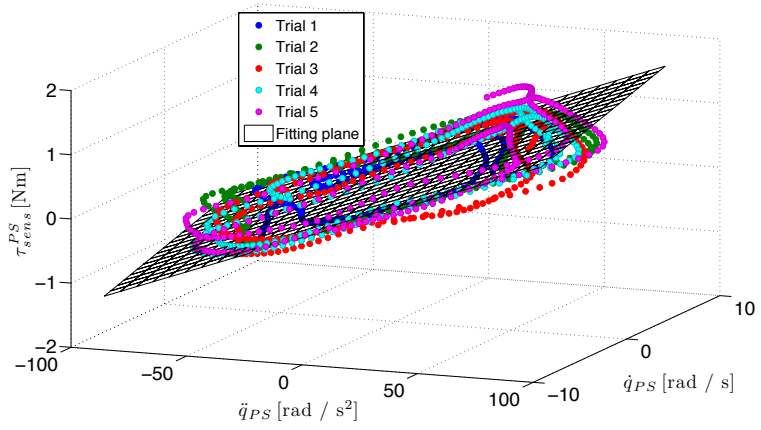

Figure 6: Multivariable linear regression for PS inertia and friction estimation as reported in (12). Considering the values averaged on 5 trials, we found $\tau_0^{PS} = 0.219 \pm 0.049$ Nm, a viscous friction $b_{PS} = 0.055 \pm 0.005$ Nm·s/rad and an inertia $B_{PS} = 0.012 \pm 0.001$ kg·m^2, with a mean R^2 of 0.942.

4 EFFECTS OF FORCE CONTROL ON ROBOT TRANSPARENCY

In this section the effectiveness of the force control in (7) in improving the transparency of the robot is tested. First, the reduction of the robot mechanical impedance in the PS joint, due to the action of the

force control has been estimated; then the reduction of forces/torques exerted by three subjects while performing two kinds of pointing tasks were analyzed, comparing the cases of *unpowered robot*, robot with *zero gains PD control*, and *force-controlled robot*.

4.1 Reduction of PS joint impedance

To evaluate the perceived robot mechanical impedance with the action of the force control, the same procedure described in section 3.2.2 was followed. In particular, the proportional gain of the force control was set to 250 $\mathrm{kg}^{-1}\mathrm{m}^{-2}$. The resultant perceived inertia should correspond to the inverse of this proportional gain (as explained in section 3) so we expect a value of 0.004 $\mathrm{kg{\cdot}m}^2$.

The multivariable linear regression reported in (12) was calculated on 5 trials; the best fitting plane is shown in Fig. 7. We found $\tau_0^{PS} = -0.059 \pm 0.043$ Nm, $b_{PS} = -0.002 \pm 0.002$ Nm·s/rad and $B_{PS} = 0.0037 \pm 0.0001$ $\mathrm{kg{\cdot}m}^2$ with a mean R^2 of 0.980.

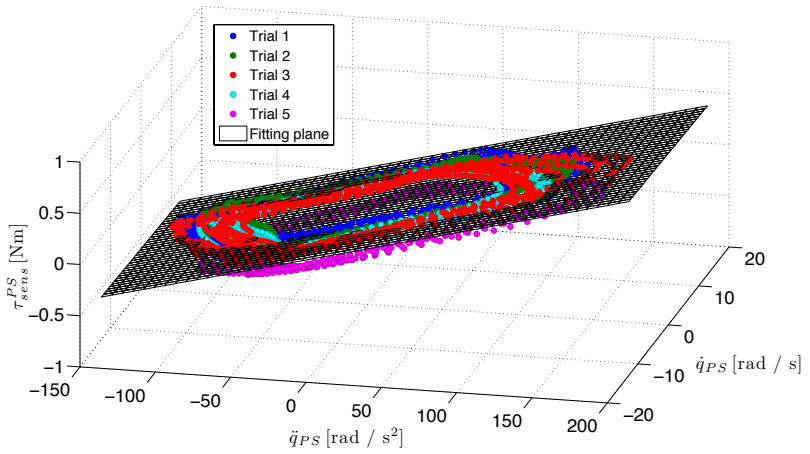

Figure 7: Multivariable linear regression for PS joint mechanical impedance estimation with force-controlled robot. Considering the values averaged on 5 trials, we found $\tau_0^{PS} = -0.059 \pm 0.043$ Nm, a viscous friction $b_{PS} = -0.002 \pm 0.002$ Nm·s/rad and an inertia $B_{PS} = 0.0037 \pm 0.0001$ $\mathrm{kg{\cdot}m}^2$, with a mean R^2 of 0.980. A reduction of about 70% of perceived inertia was obtained.

The negative value of friction suggests that an overestimation of this parameter was made. Anyway, this value can be considered negligible since it was found to be not statistically different from 0.

Of note, the implemented force control scheme in these conditions causes a reduction of the inertia of about 70% with respect to the case of PD control with gains set to zero (simple gravity compensation, as described in section 2). In particular, the estimated inertia $B_{PS} = 0.0037$ $\mathrm{kg{\cdot}m}^2$ is consistent with the expected value of 0.004 $\mathrm{kg{\cdot}m}^2$ demonstrating the effectiveness of the force control action.

4.2 Reduction of interaction forces/torques

In this section PS torques (τ_{sens}^{PS}, as in (11)) exerted by three healthy subjects (Sub1-3) to perform a 1-DOF (Pronation/Supination) task and a 3-DOFs task are reported for three different conditions: Unpowered Robot (UR), Zero gains PD control (ZPD) and Force-Controlled robot (FC).

4.2.1 Pronation/Supination (PS) task

During this 1-DOF task, three healthy subjects were asked to alternately reach 2 points displayed on a monitor on the left and right sides of a starting central point, only using the PS DOF (AA and FE DOFs were constrained in their rest positions through PD position control).

Fig. 8 shows the PS torque (11) exerted by one representative subject in the different testing conditions. The only gravity compensation (PD control with gains set to zero) reduces the torques required to perform the task with respect to the case motors are turned off; a further decrease of the torque in the case of the force-controlled robot can be noticed. Fig. 9 reports the peak and mean values of the PS torque for the 1-DOF trials on the three subjects.

It can be seen that these values slightly decrease increasing the gain K_P although no major changes occur. In case of $K_P = 300$ kg^{-1}m^{-2} the peak torque decreases of the 90% while the mean torque of the 81% with respect to the unpowered robot case. PD control only causes a reduction of the 54% and 46% of the peak and mean torques respectively. Of note, the force control ($K_P = 300$ kg^{-1}m^{-2}) reduces the peak and mean torques of 77% and 65% respectively, with respect to the PD control condition.

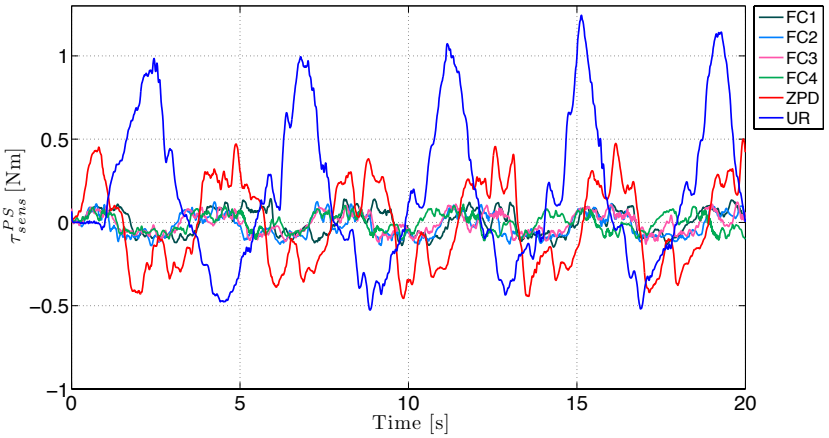

Figure 8: τ_{sens}^{PS} pattern for 1-DOF PS tasks, performed by one representative subject, in five different conditions: Unpowered Robot (UR); Zero gains PD control (ZPD); Force-Controlled robot $K_P = 150$ kg^{-1}m^{-2} (FC1); Force Control $K_P = 200$ kg^{-1}m^{-2} (FC2); Force Control $K_P = 250$ kg^{-1}m^{-2} (FC3); Force Control $K_P = 300$ kg^{-1}m^{-2} (FC4).

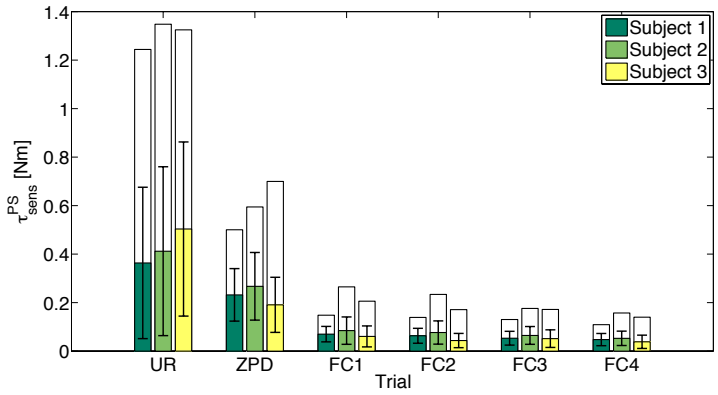

Figure 9: τ^{PS}_{sens} mean (colored) and peak (white) values for 1-DOF PS tasks on three subjects; error bars represent the standard deviation. Five conditions are reported: Unpowered Robot (UR); Zero gains PD control (ZPD); Force-Controlled robot $K_P = 150$ kg^{-1}m^{-2} (FC1); Force Control $K_P = 200$ kg^{-1}m^{-2} (FC2); Force Control $K_P = 250$ kg^{-1}m^{-2} (FC3); Force Control $K_P = 300$ kg^{-1}m^{-2} (FC4).

4.2.2 3-DOFs task

During this 3-DOFs task, three healthy subjects were asked to perform pointing movements with the wrist from the center of the workspace to 8 peripheral points arranged in a circle displayed on the monitor; this is also a typical 'video game' rehabilitation exercise (often referred as *clock* game), which has been used in [11] to test the effect of the robot on human motor strategies.

Fig. 10 shows the PS torque (11) exerted by one representative subject in the different testing conditions. Also in this case gravity compensation PD control with gains set to zero lowers the PS torques with respect to the case of unpowered robot and force control improves this effect.

Fig. 11 reports the peak and mean values of the PS torque for the trials on the three subjects. No major changes occur with the gain increasing. In case of $K_P = 300$ kg^{-1}m^{-2} the peak torque decreases of the 80% and the mean torque decreases of the 78% with respect to the unpowered robot case. PD control only decreases of the 5.6% and 5.4% the peak and mean torques respectively; thus the force control ($K_P = 300$ kg^{-1}m^{-2}) reduces the peak and mean torques of 79% and 77% respectively, with respect to the PD control condition.

An overall view of the results obtained on three subjects is presented in Table 2.

To verify that the decreasing of the interaction torques was really due to a reduction of the robot impedance and not to possible differences in the execution of the tasks during the five testing conditions, the RMS values of the velocity for the three subjects were analyzed. Results reported in Tables 3–5 show that the tasks executed by each subjects in different conditions are comparable and that the ones executed with lower velocities are actually those where the robot is in UR or ZPD conditions. These observations confirm that the reduction of the interaction torques in FC condition were due to a real reduction of robot impedance.

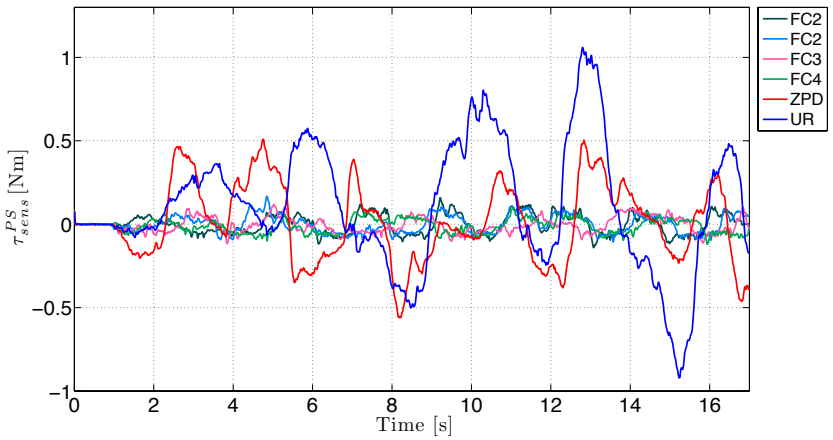

Figure 10: τ_{sens}^{PS} pattern for 3-DOFs tasks, performed by one representative subject, in five different conditions: Unpowered Robot (UR); Zero gains PD control (ZPD); Force-Controlled robot $K_P = 150$ $\text{kg}^{-1}\text{m}^{-2}$ (FC1); Force Control $K_P = 200$ $\text{kg}^{-1}\text{m}^{-2}$ (FC2); Force Control $K_P = 250$ $\text{kg}^{-1}\text{m}^{-2}$ (FC3); Force Control $K_P = 300$ $\text{kg}^{-1}\text{m}^{-2}$ (FC4).

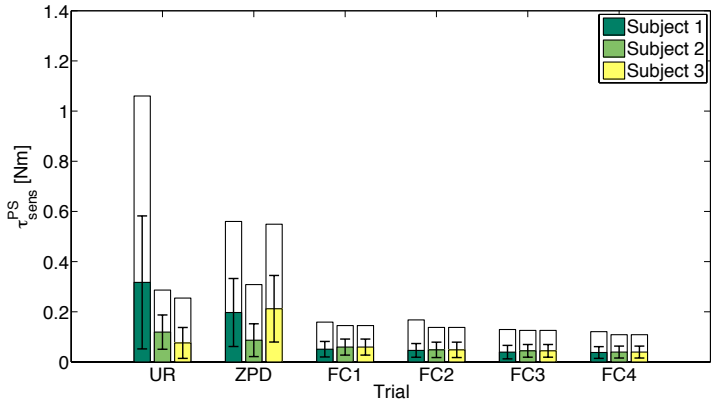

Figure 11: τ_{sens}^{PS} mean (colored) and peak (white) values for 3-DOFs PS tasks on three subjects; error bars represent the standard deviation. Five conditions are reported: Unpowered Robot (UR); Zero gains PD control (ZPD); Force-Controlled robot $K_P = 150$ $\text{kg}^{-1}\text{m}^{-2}$ (FC1); Force Control $K_P = 200$ $\text{kg}^{-1}\text{m}^{-2}$ (FC2); Force Control $K_P = 250$ $\text{kg}^{-1}\text{m}^{-2}$ (FC3); Force Control $K_P = 300$ $\text{kg}^{-1}\text{m}^{-2}$ (FC4).

Table 2: τ_{sens}^{PS} peak and mean values for PS and 3-DOFs tasks

	Peak torque [Nm]		*Mean torque* [Nm]	
	PS	3-DOFs	PS	3-DOFs
UR	1.306 ± 0.055	0.553 ± 0.441	0.427 ± 0.071	0.167 ± 0.131
ZPD	0.598 ± 0.099	0.522 ± 0.198	0.230 ± 0.038	0.158 ± 0.062
FC1	0.206 ± 0.059	0.155 ± 0.009	0.072 ± 0.012	0.056 ± 0.004
FC2	0.181 ± 0.048	0.151 ± 0.185	0.061 ± 0.017	0.049 ± 0.004
FC3	0.162 ± 0.028	0.139 ± 0.021	0.057 ± 0.007	0.043 ± 0.004
FC4	0.135 ± 0.024	0.108 ± 0.014	0.081 ± 0.066	0.037 ± 0.002

Table 3: RMS values of the velocity patterns during PS and 3-DOFs tasks [rad/s] for subject 1

	PS task	3-DOFs task		
Trial	$\dot{q}_{PS,rms}$	$\dot{q}_{FE,rms}$	$\dot{q}_{AA,rms}$	$\dot{q}_{PS,rms}$
UR	0.7062	0.3731	0.2052	0.3879
ZPD	0.8031	0.3573	0.2014	0.4664
FC1	0.7946	0.4255	0.2063	0.3356
FC2	0.7987	0.4181	0.2064	0.3085
FC3	0.8235	0.4243	0.2155	0.3761
FC4	0.8645	0.4002	0.2100	0.3455

Table 4: RMS values of the velocity patterns during PS and 3-DOFs tasks [rad/s] for subject 2

	PS task	3-DOFs task		
Trial	$\dot{q}_{PS,rms}$	$\dot{q}_{FE,rms}$	$\dot{q}_{AA,rms}$	$\dot{q}_{PS,rms}$
UR	0.7497	0.3677	0.2225	0.0431
ZPD	0.8212	0.4370	0.2545	0.0613
FC1	1.0125	0.5225	0.2790	0.1673
FC2	0.9155	0.5912	0.2870	0.3176
FC3	0.8797	0.5830	0.2938	0.2281
FC4	0.8587	0.5701	0.3055	0.3008

Table 5: RMS values of the velocity patterns during PS and 3-DOFs tasks [rad/s] for subject 3

	PS task	3-DOFs task		
Trial	$\dot{q}_{PS,rms}$	$\dot{q}_{FE,rms}$	$\dot{q}_{AA,rms}$	$\dot{q}_{PS,rms}$
UR	0.9616	0.5360	0.3263	0.0287
ZPD	0.9485	0.1258	0.0572	0.8529
FC1	1.0902	0.5225	0.2790	0.1673
FC2	0.9389	0.5912	0.2870	0.3176
FC3	0.9429	0.5830	0.2938	0.2281
FC4	1.0217	0.5701	0.3055	0.3008

4.3 Considerations on force control performance

The performance of the adopted force control scheme in general depends on the dynamic characteristics of the robot and some unstable behaviors might occur when control gains are high. This is particularly true in the case of industrial robots, where the intrinsic mechanical impedance is extremely high. Nevertheless, in our specific case the robot already presents a good level of back-drivability, so that when we implemented and tested the force control action no critical stability problems occurred.

We tested the robot with a maximum value of $K_P = 300$ kg^{-1}m^{-2}, corresponding to a very low perceived inertia (about 0.003 kg·m^2), and we did not experienced any unstable behaviors, not even when the handle was manually excited to oscillate with a peak velocity of the order of 10 rad/s and a peak acceleration of the order of 150 rad/s^2 (values which are grater than the ones normally measured during pointing tasks). Nonetheless, trials for the evaluation of human motor strategies (which will be described in the next section) were performed using a gain value lower than the maximum tested one.

In both 1-DOF and 3-DOFs tasks we found a net decrease of torques exerted by the subjects in case of force-controlled robot with respect to the PD control condition while no significant differences occurred when different gain values were used for force control. Since improving the gain values, with a fixed friction compensation, corresponds to reduce only the perceived inertia (0.007 kg·m^2 and 0.003 kg·m^2 for $K_P = 150$ kg^{-1}m^{-2} and $K_P = 300$ kg^{-1}m^{-2} respectively) it could be concluded that the major contribution in the achievement of robot transparency is given by the friction reduction (which is of course due to the direct friction compensation but also to the force feedback).

Moreover, considering a perfect estimation of gravity and friction terms, from (1) and (2) it can be seen that the force error dynamics becomes:

$$\boldsymbol{e}_f = \frac{\boldsymbol{B}}{\hat{\boldsymbol{B}}\boldsymbol{K_P}}\ddot{\boldsymbol{q}} \tag{13}$$

It is worth recalling that $\boldsymbol{B}$ represents robot inertia, $\hat{\boldsymbol{B}}$ is its estimation and $\ddot{\boldsymbol{q}}$ is the vector of joints accelerations.

Equation (13) shows that an error in the inertia estimation is compensated by the proportional gain. If inertia is overestimated the force control gain has to be reduced of the same amount to preserve the stability margin, while if inertia is underestimated the gain can be incremented. From a different perspective we can say that the responsible of the stability is the product $\hat{\boldsymbol{B}}\boldsymbol{K_P}$ so that a variation of the gain make the control law basically insensible to inertia estimation.

5 HUMAN MOTOR STRATEGIES DURING POINTING TASKS

In this section we analyze pointing tasks of three subjects in three different operative conditions. Firstly wrist rotations were recorded using a handheld device that introduced a negligible loading effect (in this condition subjects movements were basically free); these results were compared with the ones obtained during the interaction with the robot when the gains of its standard PD control scheme were set to zero and when the proposed force control was active. Since the zero gains PD control actually corresponds to only gravity compensation, the comparison with the force-controlled robot allows to evaluate the effect of inertia and friction compensation.

For each condition the experimental protocol included five learning trials, that were used to make the subjects acquainted with the experimental setup, and five trials to be used for data analysis.

5.1 Analysis of wrist movements during pointing tasks

5.1.1 Handheld device

To assess natural motor strategies during pointing task with the wrist, we used a 'video game' showing to subjects some visual targets to be reached (from/to a central target to/from peripheral ones) (Fig. 12); this protocol has been already used to assess the existence of Donders' law for the wrist during pointing tasks [16].

The subject under test was seated on a chair and rested his arm on a support purposively created to bind arm and forearm (Fig. 13). In this way she/he could execute pointing tasks moving only the wrist.

Each trial started after defining a *primary position* (see [16] for details); the subject was then instructed to move the round cursor on the screen towards the peripheral positions randomly chosen by the software among 1, 2, ..., 8 (Fig. 12) and then back to the central position. To register the wrist movements we instrumented an hollow cylindrical handle (height: 150 mm; outer diameter: 50 mm; inner diameter: 35 mm; mass: 120 g) with an inertial magnetic unit (IMU, MTx-28A53G25 device from XSens Inc. - angular resolution: 0.05 deg; static orientation accuracy: < 1 deg; dynamic accuracy: 2 deg RMS; bandwidth: 40 Hz); this setup is indicated as *handheld device* (Fig. 13).

With the wrist in its primary position, a fixed reference frame $\{x_0, y_0, z_0\}$ was defined (see Fig. 13): z_0-axis is along the vertical direction (upwards), x_0-axis is horizontal and aligned with the forearm (forward) and y_0-axis is horizontal and perpendicular to the forearm (leftward). A second (moving)

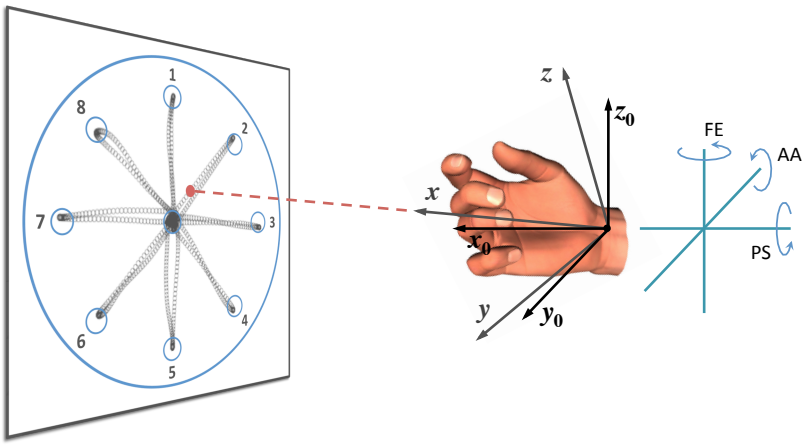

Figure 12: Typical 'video game' used to guide subject to perform pointing tasks (left) and a representation of the three wrist DOFs and of the reference frames (right).

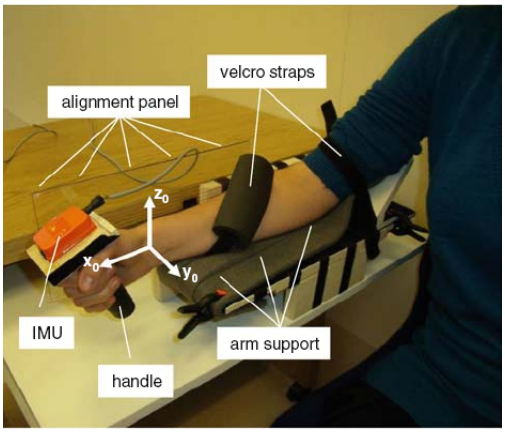

Figure 13: Experimental apparatus for trials with handheld device.

reference frame $\{x, y, z\}$ attached to the wrist (see also Fig. 12) was defined to coincide with the fixed reference frame when the wrist is in the primary position.

The IMU, connected to a PC, was configured to continuously acquire a rotation matrix $\boldsymbol{R}$ (at a rate of 100 samples/s) which expresses the orientation of the wrist moving frame with respect to the fixed frame.

We calculated the rotation vector as:

$$\boldsymbol{r} = \frac{\theta}{2\sin(\theta)} \begin{bmatrix} R_{3,2} - R_{2,3} \\ R_{1,3} - R_{3,1} \\ R_{2,1} - R_{1,2} \end{bmatrix} \tag{14}$$

where $R_{j,k}$ indicates the (j,k) element of the matrix $\boldsymbol{R}$ and $\theta = \arccos[(\text{trace}(\boldsymbol{R}) - 1)/2]$, being $\text{trace}(\boldsymbol{R}) = R_{1,1} + R_{2,2} + R_{3,3}$ and $|\theta| < \pi$. The vector $\boldsymbol{r}$ defines the axis (parallel to $\boldsymbol{r}$ itself) and the amount of rotation ($\|\boldsymbol{r}\| = \theta$).

Since the primary position was selected as the 'home' position for the IMU the coordinates of the x–, y–, and z–axis with respect to the fixed frame could be determined, respectively, as the first, the second, and the third columns of the matrix $\boldsymbol{R}$. For this reason the pointing vector $\boldsymbol{n}$ (which represents the pointing direction during the tasks) was always parallel to the moving x-axis after the reset procedure and it could be determined as follows:

$$\boldsymbol{n} = \boldsymbol{R}\ [1\ 0\ 0]^T \tag{15}$$

While the three components of a rotation vector $\boldsymbol{r}$, in general, define points of a 3-dimensional space, the wrist pointing vectors $\boldsymbol{n}$ necessarily lie in a 2-dimensional space.

Considering the subscript i to represent the i-th acquisition sample, the temporal sequence of acquired rotation matrices and of the derived rotation and pointing vectors can be indicated as $\boldsymbol{R}_i$, $\boldsymbol{r}_i$ and $\boldsymbol{n}_i$ respectively.

Numerically, the sequence $\boldsymbol{r}_i = [r_{xi}\ r_{yi}\ r_{zi}]^T$ was fitted to $\boldsymbol{r}_i^* = [r_{xi}^*\ r_{yi}\ r_{zi}]^T$ where r_{xi}^* is defined by a generic quadratic surface:

$$r_{xi}^* = C_1 + C_2 r_{yi} + C_3 r_{zi} + C_4 r_{yi}^2 + 2C_5 r_{yi} r_{zi} + C_6 r_{zi}^2 \tag{16}$$

where the coefficients $C_1, \ldots, C_6$ were determined via least-squares fitting methods. The first three coefficients (C_1, C_2 and C_3) define a plane, while the last three coefficients (C_4, C_5 and C_6) are related to the curvature of the fitted surface. In particular, the coefficient C_5 denotes the amount of twisting of a quadratic surface.

Fig. 14 reports an example for the graphical representation of the temporal sequences of rotation and pointing vectors ($\boldsymbol{r}_i$ and $\boldsymbol{n}_i$). Remarkably, it can be observed that the rotation vectors tend to lie on a 2-dimensional (Donders') surface (represented by equation (16)), which can also be well approximated by a plane near the primary position.

As in previous studies [11, 16], the thickness of a Donders' surface is defined as the standard deviation of the fitting error between the sequence $\boldsymbol{r}_i$ and the best fitting surface. For a given set of fitting coefficients ($C_1, \ldots, C_6$), the fitting error is defined as $r_{xi} - r_{xi}^*$.

Obviously, thickness values quantify the goodness of fitting and indicate how much the rotation vectors tend to lie on the best fitting surface (Donders' surface); low values of thickness indicate that a soft constraint (such as Donders' law) apply to wrist kinematics during pointing tasks. As an example, both sequences of a single trial are plotted in Fig. 14. While the wrist pointing directions necessarily lie in a 2-dimensional space, the three components r_{xi}, r_{yi} and r_{zi} of a rotation vector $\boldsymbol{r}_i$, in general, define points of a 3-dimensional space. Remarkably, it can be observed that the rotation vectors tend to lie on a 2-dimensional surface (Donders' law), which can be well approximated by a plane near the 'zero' position (Fig. 14).

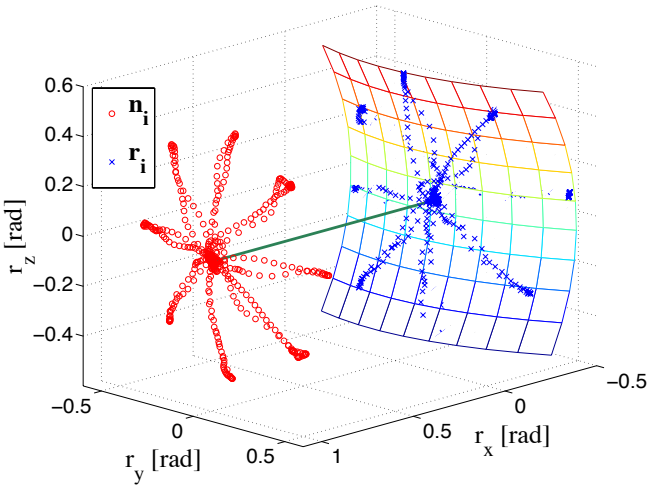

Figure 14: Rotation vectors (blue crosses) are represented in the 3-dimensional space of the motor task together with the pointing vectors (red circles). A 2-dimensional quadratic surface fits the rotation vectors. The green straight line represents the pointing direction when the wrist is in the primary position.

5.2 Wrist robot

Subjects were strapped to a chair with their right arm fasten to the InMotion[3] arm-support by appropriate belts to minimize torso, shoulder and elbow movements; in this configuration only wrist rotations were left unconstrained while the subject grasps the handle of the robot (Fig. 15). The more distal strap only constraints the flexion of the elbow while allowing a free pronation/supination movement. In this way the PS joint is moved by the user only exerting forces on the handle and not via the strap.

For the experiments described in this section, two different conditions were tested: in the first one, the motors of the robot were commanded so that they only compensate gravity, with the stiffness and damping parameters of the native impedance controller set to zero; in the second one, subjects performed the same task with the robot controlled using the force control law in (2). In what follows we refer to these two operative conditions as *zero gains PD control* and *force-controlled robot* respectively.

The starting position for the wrist was set as to coincide with the mechanical zero position of the robot, defined in [17]. Knowledge of the sequence, from proximal to distal, of the mechanical joints allows to determine the wrist orientation $\boldsymbol{R}_w$ from the angles as sensed by the encoders of the system:

$$\boldsymbol{R}_w = \boldsymbol{R}_x\left(\theta_{PS}\right)\boldsymbol{R}_y\left(\theta_{AA}\right)\boldsymbol{R}_z\left(\theta_{FE}\right) \tag{17}$$

where x, y and z coincide with the axes of the fixed reference frame. i.e. the primary or 'zero' position for the wrist. For a given wrist orientation $\boldsymbol{R}_w$, the wrist pointing direction $\boldsymbol{n}_i$ is given as in (15). During the execution of each task, data were acquired at a rate of 200 Samples/sec, in particular the three sequences of sampled angles, and (where i refers to i-th sample at time t_i). Using eq. (17), the sequence of wrist orientation $\boldsymbol{R}_{wi}$ at time t_i was derived. The sequence of wrist pointing directions

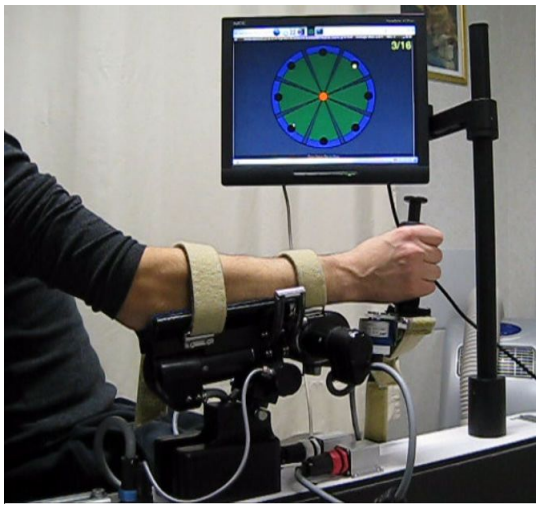

Figure 15: Experimental set up for trials with InMotion^3 system.

$\boldsymbol{n}_i$ was evaluated via (15) and finally the sequence of rotation vectors $\boldsymbol{r}_i$ was obtained via (14). The sequence $\boldsymbol{r}_i = [r_{xi}\ r_{yi}\ r_{zi}]^T$ was numerically fitted to a generic quadratic surface with coefficients C_1, $\ldots, C_6$ as in (16).

5.3 Free movements and human-robot interaction: a comparison

Donders' surfaces are typically subject-dependent and reveal personal motor strategies, as demonstrated in previous studies [16]. The effect of a purely mechanical (holonomic) constraint on a 3-DOFs wrist mechanism, e.g. a locked joint, is to constrain the system configuration exactly to a 2-dimensional surface. Noisy measurements and mechanism non-idealities (e.g. backlash) would reveal such a surface with a certain resolution, for the robotic systems under consideration this is (often much) less than 0.1 deg. Observing a mechanically unconstrained 3-DOFs system evolving on a subspace (2-dimensional surface) of its configuration space (3-dimensional) is indicative of active control. This has been attributed to a form of neural control in studies relative to the oculomotor system [12] and to the upper limbs [14, 15, 16]. Unlike physical constraints, neural control is characterized by much larger variability (or 'biological noise' [12]) leading to thicknesses in the order of 1–3 deg [12, 14].

In this section we reported the results obtained in the three different experimental conditions, namely experiments with the handheld device, with the robot in zero gains PD control mode and with the force-controlled robot. In Figs. 16, 17 the Donders' surfaces and the histograms of the mean values of C_1, $\ldots$, C_6 coefficients are reported.

In the experiments when the handheld device was used, neural kinematic constraints arose as 2-dimensional surfaces embedded in the 3-dimensional space of wrist configurations. The lightness of the handheld device allows the subjects' own motor style to emerge: different trials show similar curvature for the same subject, while they differ among subjects, as already proved in [11, 16]. During the interaction of subjects with the robot in zero gains PD control mode the high goodness-of-fit in terms of

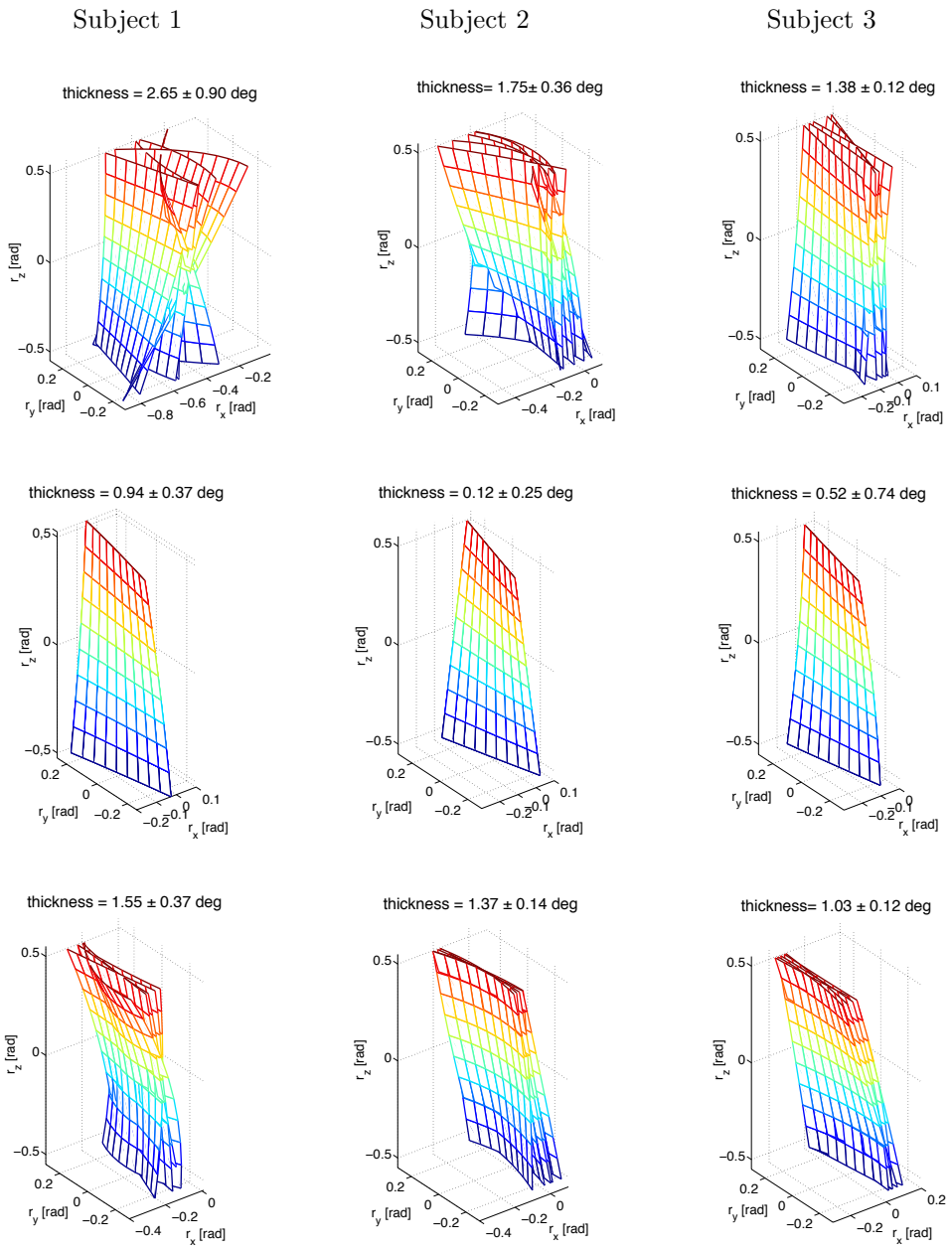

Figure 16: Donders' surfaces fitting the rotation vectors (in radians) relative to three different subjects who perform the same pointing task, each one composed of 5 trials, in three different operative way: with handheld device (top), with robot in zero gains PD control mode (middle), with force-controlled robot (bottom).

Table 6: Thickness values in radians

Subject	Handheld device	Robot with PD control (zero gains)	Force-controlled robot
1	0.031 ± 0.006	0.016 ± 0.007	0.024 ± 0.002
2	0.046 ± 0.016	0.002 ± 0.004	0.027 ± 0.006
3	0.024 ± 0.002	0.009 ± 0.013	0.018 ± 0.002
overall	0.034 ± 0.008	0.009 ± 0.008	0.023 ± 0.003

thickness (1-2 order of magnitude smaller than in the experiments with the handheld device) revealed the strong influence of robot in covering the human motor strategies. In this case 2-dimensional surfaces are similar for all subjects highlighting the absence of any biological noise (Fig. 16). It has to be noticed that, since the the robot constraining behavior has also been verified in [11] (where experiments were conducted without any modification to the mechanical structure of the system), the perturbation to the human natural motor strategies cannot be due to the removal of the passive revolute joint and of the linear slider.

In the case of force-controlled robot, 2-dimensional surfaces were different among tested subjects; moreover, each subject' surfaces were similar to those coming from the experiment with the handheld device, with thickness values got back into the physiological range (1–3 deg). From the analysis of the coefficients C_4, C_5 and C_6, which are related to Donders' surfaces curvature, no discrepancy between the values measured with the handheld device and with the force controlled robot emerges. This confirms the analogies between the two performances.

The constraining action of the robot, when controlled through the PD control (with gains set to zero) is particularly evident in the Helmholtz-like behavior of the surfaces: the sign of the C_5 coefficient is inter-subjectively invariant and positive. It is worth recalling that the Helmholtz gimbal is a 2-dimensional mechanism and its rotation vectors necessarily lie on a 2-dimensional surface; in the case the surface is expressed through the (16) this implies $C_5 = 1/2$ and all the other coefficients to be zero. The explanation to this result is that subjects natural movements are affected by an excessive mechanical impedance on the PS joint of the robot; this is confirmed by the restoration of a natural behavior during the execution of the tasks with a more transparent robot (from Table 6 it can be seen that thickness values became physiological) and by an evident activation of PS DOF.

6 CONCLUSIONS

The paper addresses not only the traditional issues of pHRI (physical Human-Robot Interaction) in terms of safety and biomechanical compatibility but also the problem of coping with human motor strategies and neural mechanisms adopted to solve redundancy during motor tasks which are not appropriately considered in the design of actual robotic systems.

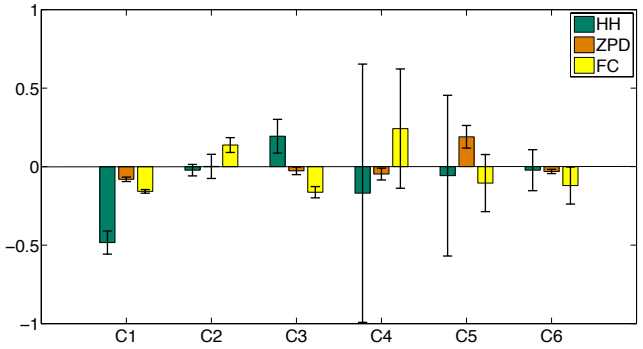

(a)

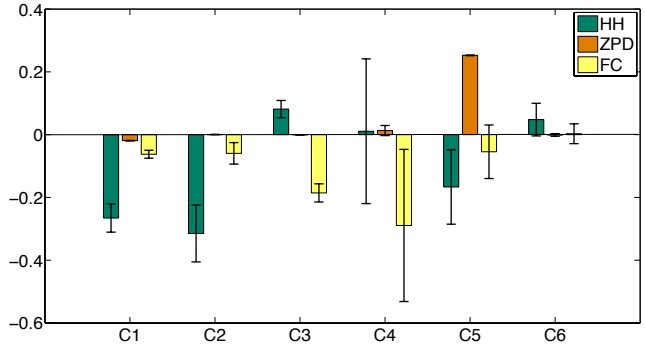

(b)

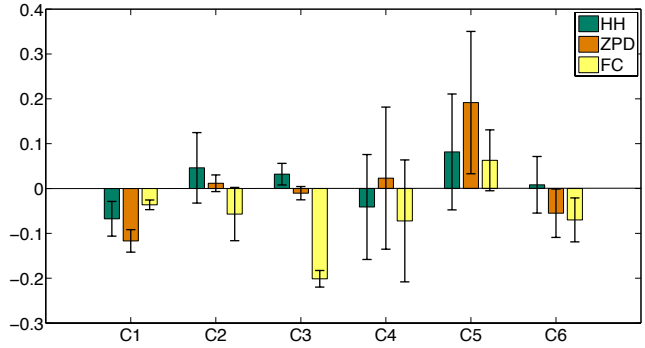

(c)

Figure 17: Histograms of the $C_1, \ldots, C_6$ coefficients (averaged on 5 trials, the vertical bars represent the 95% confidence interval) each of one relative to a single subject in 3 different operative conditions; (a) Subject 1, (b) Subject 2, (c) Subject 3. (HH: HandHeld device; ZPD: robot in Zero gains PD control mode; FC: Force-Controlled robot).

Previous studies reported the existence of neural constraints for the human wrist during kinematically redundant tasks and also showed how such motor strategies can be perturbed when subjects interact with a state-of-the-art wrist robot, despite its high level of back-drivability [11, 16].

It was hypothesized that the robot mechanical impedance associated with the PS joint could be directly responsible for the perturbation of the natural motor strategies. For this reason in this work we implemented a basic control scheme, specifically for the PS axis, to reduce the human-robot interaction forces and to study the effects of a lower perceived impedance on such neural constraints. From the analysis of Donders' surfaces associated to the execution of pointing tasks we found that, when interacting with the force-controlled robot, subjects regained natural motor behaviors as during free pointing (measured with a lightweight handheld device).

The work emphasizes the possibility of minimizing the perturbation to human natural motion even through simple solutions like a well known direct force control approach. This represents the starting point towards new scenarios for the design of rehabilitation robots, that at the state of art do not consider neural constraints but only biomechanical ones. In this regard, our future work will aim at investigating which is the range of impedance values that allows to fully cope with neural constraints; to the authors' knowledge this aspect has not been analyzed yet and it can represent an important criteria for robot design.

ACKNOWLEDGMENTS

This work was partly funded by the FP7 FET Proactive Initiative "Embodied Intelligence", project no. ICT-2007.8.5-231451 - EVRYON, by the FP7 ICT project no. ICT-2007.3.2-231722 - IM-CLeVeR and by the Academic Research Fund (AcRF) Tier1 (RG 40/09), Ministry of Education, Singapore.

REFERENCES

[1] H. I. Krebs, N. Hogan, M. L. Aisen, B.T. Volpe, Robot-aided neurorehabilitation, *IEEE Transactions on Rehabilitation Engineering*, **6**, pp. 75-87 (1998).

[2] H. I. Krebs, M. Ferraro, S. Buerger, M. J. Newbery, A. Makiyama, M. Sandmann, D. Lynch, B. T. Volpe, and N. Hogan, Rehabilitation robotics: Pilot trial of a spatial extension for MIT-Manus, *IEEE Trans. Neural Syst. Rehabil. Eng.*, **15**, pp. 327-335 (2007).

[3] C. G. Burgar, P. S. Lum, P. C. Shor, and H. F. M. Van der Loos, Development of robots for rehabilitation therapy: The Palo development of robots for rehabilitation therapy: The Palo Alto Stanford experienc, *Journal of rehabilitation research and development*, **37**, pp. 663-673 (2000).

[4] P. S. Lum, D. J. Reinkensmeyer, R. Mahoney, W. Z. Rymer, and C. G. Burgar, Robotic devices for movement therapy after stroke: Current status and challenges to clinical acceptance, *Topics in stroke rehabilitation*, **8**, pp. 40-53 (2002).

[5] D. J. Reinkensmeyer, L. E. Kahn, M. Averbuch, A. McKenna-Cole, B. D. Schmit, and W. Z. Rymer, Understanding and treating arm movement impairment after chronic brain injury: Progress with the arm guide, *J. Rehabil. Res. Dev.*, **37**, pp. 653-662 (2000).

[6] L. E. Kahn, M. L. Zygman, W. Z. Rymer, and D. J. Reinkensmeyer, Robot-assisted reaching exercise promotes arm movement recovery in chronic hemiparetic stroke: A randomized controlled pilot study, *J. Neuroeng. Rehabil.*, **3**, (2006).

[7] G. Colombo, R. Riener, and L. Lünenburger, Human-centered robotics applied to gait training and assessment, *Journal of rehabilitation research and development*, **43**, pp. 679-694 (2006).

[8] J. D. Schaechter, Motor rehabilitation and brain plasticity after hemiparetic stroke, *Prog. Neurobiol.*, **73**, pp. 61-72 (2004).

[9] R. Teasell, N. A. Bayona, J. Bitensky, Plasticity and reorganization of the brain post stroke, *Topics in Stroke Rehabilitation*, **12**, pp. 11-26 (2005).

[10] D. Reinkensmeyer, N. Hogan, H. I. Krebs, S. L. Lehman, P. S. Lum, Rehabilitators, robots and guides: new tools for neurological rehabilitation, in *Biomechanics and Neural Control of Posture and Movement*, J. Winters, P. E. Crago (Eds.), pp. 516-534, Springer-Verlag (2000).

[11] D. Campolo, D. Accoto, D. Formica, E. Guglielmelli, Intrinsic constraints of neural origin: Assessment and application to rehabilitation robotics, *IEEE Transaction on Robotics*, **25**, pp. 492-501 (2009).

[12] D. Tweed and T. Vilis, Geometric Relations of Eye Position and Velocity Vectors during Saccades,*vision Res.*, **30**, pp. 111-127 (1990).

[13] A. M. F. Wong, Listing's law: Clinical significance and implications for neural control, *Surv. Ophthalmol.*,**49**, pp. 563-575 (2004).

[14] D. G. Liebermann, A. Biess, J. Friedman C. C. A. M. Gielen, T. Flash, Intrinsic joint kinematic planning. I: Reassessing the Listing's law constraint in the control of three-dimensional arm movements, *Exp. Brain. Res.*, **171**, pp. 139-154 (2006).

[15] M. Fetter, T. Haslwanter, H. Misslich, D. Tweed, *Threedimensional Kinematics of the Eye, Head and Limb Movements*, Harwood Academic Publisher, Amsterdam, (1997).

[16] D. Campolo, D. Formica, E. Guglielmelli, F. Keller, Kinematic analysis of the human wrist during pointing tasks, *Experimental Brain Research*, **201**, pp. 561-573 (2010).

[17] H. I. Krebs, B. T. Volpe, D. Williams, J. Celestino, S. K. Charles, D. Lynch and N. Hogan, Robot-aided neurorehabilitation: a robot for wrist rehabilitation, *IEEE Transactions on Rehabilitation Engineering*, **15**, pp. 327-335 (2007).

[18] N. L. Tagliamonte, D. Formica, D. Campolo, E. Guglielmelli, Coping with Intrinsic Constraints of Neural Origin in the Design of Rehabilitation Robots: a Preliminary Study, in *Proc. International IEEE/EMBS Conference on Neural Engineering*, Antalya, pp. 124-127 (2009).

[19] O. Khatib, Inertial properties in robotics manipulation: an object-level framework, *International Journal of Robotics Research*, **14**, pp. 19-36 (1995).

[20] R. Volpe, P. Khosla, A theoretical and experimental investigation of explicit force control strategies for manipulators, *IEEE Trans. Autom. Control*, **38**, pp. 1634-1650 (1993).

[21] R. M. Murray, Z. Li, and S. S. Sastry, *A Mathematical Introduction to Robotic Manipulation*, CRC Press, Boca Raton, FL (1994).